SCIENCE CHINA
Chemistry

•ARTICLES•

May 2024 Vol.67 No.5: 1596–1604
https://doi.org/10.1007/s11426-024-1948-6

Delicate chemical structure regulation of nonfullerene acceptor for efficient and large thickness organic solar cells

Zhe Zhang[1†], Wanying Feng[1†], Yunxin Zhang[2], Shaohui Yuan[2], Yuyang Bai[2], Peiran Wang[1], Zhaoyang Yao[1*], Chenxi Li[1], Tainan Duan[3], Xiangjian Wan[1], Bin Kan[2*] & Yongsheng Chen[1*]

[1]*State Key Laboratory and Institute of Elemento-Organic Chemistry, Frontiers Science Center for New Organic Matter, The Centre of Nanoscale Science and Technology and Key Laboratory of Functional Polymer Materials, Renewable Energy Conversion and Storage Center (RECAST), College of Chemistry, Nankai University, Tianjin 300071, China;*
[2]*School of Materials Science and Engineering, National Institute for Advanced Materials, Nankai University, Tianjin 300350, China;*
[3]*Chongqing Institute of Green and Intelligent Technology, Chongqing School, University of Chinese Academy of Sciences (UCAS Chongqing), Chinese Academy of Sciences, Chongqing 400722, China*

Received January 4, 2024; accepted February 2, 2024; published online April 9, 2024

Inspired by the success of CH-series acceptors, a small-molecular acceptor, CH-Tz was reported by adopting a new conjugation-extended electron-deficient unit ([1,2,5]thiadiazolo[3,4-b]pyrazine) on the central core. Owing to the enhanced inter-/intramolecular interactions, CH-Tz exhibited near-infrared absorption and an effective three-dimensional molecular packing network in its single crystal. When blended with polymer donor PM6, the binary device achieved a high power conversion efficiency (PCE) of 18.54%, with a notable short-circuit current density (J_{sc}) of 27.54 mA cm^{-2} and an excellent fill factor (FF) over 80%, which can be partly ascribed to the balanced charge transport properties in the blend film. After employing D18-Cl as the third component, an enhanced PCE of 18.85% was achieved due to a more obvious fiber network. Impressively, the CH-Tz-based OSC devices show excellent thermal stability and thickness insensitivity. Record-breaking J_{sc} of 28.92 mA cm^{-2} was reached for PM6:D18-Cl:CH-Tz ternary device with a thickness of 560 nm. Besides, CH-Tz shows potential in fabricating multicomponent high-performance organic solar cells, where over 19% efficiency could be realized in the quaternary device. Our work advances the strong influence of electron-deficient central units on molecular photovoltaic properties and guides the design of acceptors for stable and large-thickness organic solar cells.

organic solar cells, non-fullerene acceptor, central unit, large thickness, molecular packing

Citation: Zhang Z, Feng W, Zhang Y, Yuan S, Bai Y, Wang P, Yao Z, Li C, Duan T, Wan X, Kan B, Chen Y. Delicate chemical structure regulation of nonfullerene acceptor for efficient and large thickness organic solar cells. *Sci China Chem*, 2024, 67: 1596–1604, https://doi.org/10.1007/s11426-024-1948-6

1 Introduction

Organic solar cells (OSCs) are regarded as one of the most promising candidates for generating sustainable energy owing to their merits, including solution-processability, ultra-flexibility, and semitransparency [1–5]. Recently, the emergence of acceptor-donor-acceptor (A-D-A)-type nonfullerene acceptors (NFAs) has prompted the rapid development of OSCs. In particular, Y-series acceptor-based devices have achieved power conversion efficiencies (PCEs) exceeding 19% and 20% in single-junction and tandem OSCs, respectively [6–14]. Compared with traditional A-D-A NFAs (for example, 3,9-bis(2-methylene-(3-(1,1-dicyanomethylene)-indanone))-5,5,11,11-tetrakris(4-hexylphenyl)-dithieno[2,3-d:2′,3′-d′]-*s*-indaceno[1,2-b:5,6-b′]

†These authors contributed equally to this work.
*Corresponding authors (email: yschen99@nankai.edu.cn; kanbin04@nankai.edu.cn; zyao@nankai.edu.cn)

dithiophene (ITIC) analogs), the most significant character of Y6 is that its central unit, benzo[*c*][1,2,5]thiadiazole (BT), participates in molecular packing, leading to an effective three-dimensional (3D) intermolecular packing network [15–18]. Owing to such unique molecular packing behaviors, efficient charge carrier transport and relatively low exciton binding energy could be realized in Y-series-based devices. These advantages make it possible to simultaneously obtain a high short-circuit current density (J_{sc}) with a low energy loss (E_{loss}) [7,19–22]. This provides a pathway for resolving the dilemma of the trade-off between the open-circuit voltage (V_{oc}) and J_{sc} in OSCs [23].

Inspired by the crucial role of the central unit in Y6, our group developed CH-series acceptors with 2D conjugation extended central units [24,25]. The 2D conjugation extension of CH-series acceptors offers a more rigid molecular skeleton, which is beneficial for reducing the vibration of the molecular skeleton and increasing the photoluminescence quantum yield [26]. Single crystal X-ray diffraction (XRD) has revealed that CH-series acceptors exhibit more effective and compact 3D molecular packing compared with that of Y6 [24,27]. Owing to the efficient charge dynamics and reduced nonradiative recombination losses of CH-based devices, these types of acceptors have become very promising for improved OSC devices. Presently, the PCE of devices based on CH-series acceptors has exceeded 19% with a high V_{oc} of 0.909 V [28]. Recently, we employed the conjugate expansion of central units to design and synthesize CH-BQ (Figure S1, Supporting Information online), CH-iBQ, and CH-BBQ to study the impact of electron-deficient units (*e.g.*, benzothiadiazole) on photovoltaic performance [29]. PM6:CH-iBQ and PM6:CH-BBQ binary OSCs achieved PCEs of 18%. However, PM6:CH-BQ-based devices exhibited an inferior PCE of 12.85%. Considering that CH-BQ still had a narrow optical bandgap and suitable energy level, it was still possible to obtain efficient NFAs if the CH-BQ molecular skeleton was properly adjusted. Comparing CH-BQ with CH_4 (Figure S1) [25], it was observed that the binary devices prepared using CH_4 without thiadiazole in the central unit could achieve a satisfactory PCE of 16.49%. This implies that the appropriate reduction of the central core is conducive to improving the photovoltaic performance of NFA devices.

Based on CH-BQ and CH_4, we wondered if better performance might be achieved if benzene was removed from the central unit. Thus, we designed and synthesized an NFA of (2,2′-((2Z,2′Z)-((14,15-bis(2-hexyldecyl)-3,11-diundecyl-14,15-dihydro-[1,2,5]thiadiazolo[3,4-b]thieno[2″,3″:4′,5′]thieno[2′,3′:4,5]pyrrolo[3,2]fthieno[2″,3″:4′,5′]thieno[2′,3′:4,5]pyrrolo[2,3-h]quinoxaline-2,12diyl)bis(methaneylylidene))bis(5,6-dichloro-3-*oxo*-2,3-dihydro-1*H*-indene-2,1-diylidene))dimalononitrile) (CH-Tz). The central position of CH-Tz featured a conjugation extended electron-deficient core of [1,2,5]thiadiazolo[3,4-b]pyrazine. The narrow optical band gap, suitable energy levels, and proper miscibility of CH-Tz with PM6 enable broad absorption abilities and optimal morphological characteristics in PM6:CH-Tz blends. Consequently, a J_{sc} of 27.54 mA cm^{-2} and an excellent fill factor (FF) above 80% can enable a high PCE of 18.54% for PM6:CH-Tz-based OSCs. To further improve the photovoltaic performance, D18-Cl with a deep highest occupied molecular orbital (HOMO) polymer was added to regulate the crystallinity of the blend film, thereby tuning the morphology of the active layer. The blend films of PM6:D18-Cl:CH-Tz formed a more evident fiber network and a more ordered molecular aggregation. This led to more efficient exciton dissociation, faster charge transportation, less charge recombination, and reduced energy loss. Thus, PM6:D18-Cl:CH-Tz ternary OSCs exhibited an enhanced PCE of 18.85% with a V_{oc} of 0.842 V, a J_{sc} of 28.15 mA cm^{-2}, and an FF of 79.45%. CH-Tz-based devices exhibited outstanding thermal stability, maintaining 85% of their initial PCE after 630 h under continuous heating at 65 °C without encapsulation in a nitrogen-filled glove box. Owing to the FF of the CH-Tz-based devices, a high PCE of 14.93% and an unprecedented J_{sc} of 28.92 mA cm^{-2} were achieved when the thickness of the active layers was 560 nm. The excellent thermal stability and thick film tolerance of CH-Tz rendered it ideal for industrialization. Finally, a PCE exceeding 19% was realized by incorporating L8-BO into PM6:D18-Cl:CH-Tz to fabricate quaternary devices, suggesting the universality of CH-Tz in fabricating multi-component OSCs.

2 Results and discussion

Figure 1a shows the molecular structure of CH-Tz, and Scheme S1 (Supporting Information online) shows the corresponding synthesis route. Generally, the most challenging task is the construction of a large-fused ring core with the new 2D conjugation extended central unit (compound **2**). This could be successfully synthesized from 11,12-bis(2-hexyldecyl)-3,8-diundecyl-11,12-dihydrothieno[2″,3″:4′,5′]thieno[2′,3′:4,5]pyrrolo[3,2-g]thieno[2′,3′:4,5]thieno[3,2-b]indole-5,6-dione (compound **1**) and 1,2,5-thiadiazole-3,4-diamine. The diketone, compound **1**, was prepared following our developed methods [29]. The two subsequent steps encompass the Vilsmeier-Haack reaction, followed by Knoevenagel condensation, which afforded the targeted molecular CH-Tz in high yields. The chemical structures of these intermediates and CH-Tz were verified by nuclear magnetic resonance spectroscopy and high-resolution matrix-assisted laser desorption/ionization-time of flight (MALDI-TOF) mass spectrometry. Based on density functional theory calculation results (Figure 1b), the molecular skeleton of CH-Tz

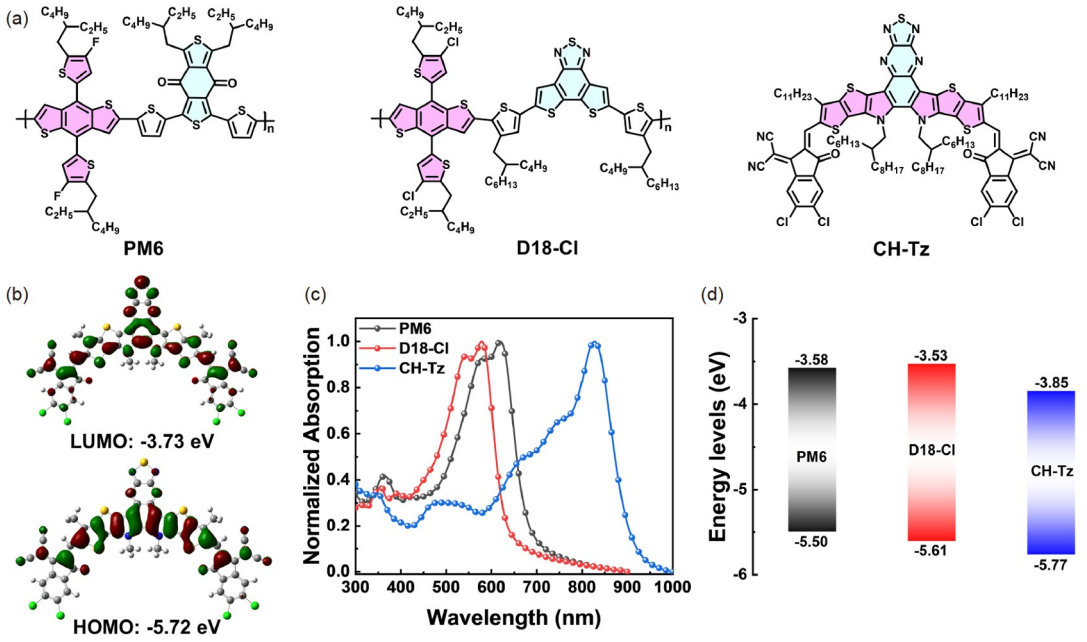

Figure 1 (a) The molecular structures of PM6, D18-Cl and CH-Tz, respectively. (b) Theoretical density distribution for the frontier molecular orbits of CH-Tz. (c) The normalized absorption spectra of PM6, D18-Cl and CH-Tz in neat film. (d) The energy level diagrams of PM6, D18-Cl and CH-Tz (color online).

was slightly twisted because of the alkyl groups attached to the nitrogen atom. The HOMO is mainly located along molecular backbones. The strong electron-withdrawing central core causes the distribution of the lowest unoccupied molecular orbital (LUMO) to be located in the central unit and molecular backbone. The calculated HOMO and LUMO energy levels of CH-Tz were −5.72 and −3.73 eV, respectively. The calculated electrostatic surface potential (ESP) maps of CH-Tz are displayed in Figure S2. Both the central unit and end group possessed negative ESP values, further echoing the strong electron-withdrawing property of the central core.

Figure 1c and Figure S3a show the normalized ultraviolet-visible (UV-vis absorption spectra of PM6, D18-Cl, and CH-Tz in a diluted chloroform solution and neat film. The maximum absorption peak of CH-Tz in the diluted chloroform solution and the neat film was observed at 755 and 828 nm, respectively. The near-infrared absorption characteristic of CH-Tz at an absorption onset of 905 nm led to its low optical bandgap of 1.37 eV. Encouragingly, CH-Tz exhibited a large redshift ($\Delta\lambda$) of 73 nm when transforming from solution into film, indicating an effective intermolecular π-π stacking for CH-Tz [30]. CH-Tz also showed a large maximum coefficient of 6.2×10^5 M^{-1} cm^{-1} in solution and 1.1×10^5 cm^{-1} in film, indicating its strong light harvesting capacity. Figure S3b shows the normalized UV-vis absorption spectra of the blend films of PM6:CH-Tz, D18-Cl:CH-Tz, and PM6:D18-Cl:CH-Tz. The main absorption peak of CH-Tz in the blend films of D18-Cl:CH-Tz exhibited a redshift of 4 nm, compared with that of PM6:CH-Tz. This indicated that CH-Tz formed a more ordered molecular aggregation in the blend film of D18-Cl:CH-Tz [31–33]. Cyclic voltammetry was performed to evaluate the energy levels of PM6, D18-Cl, and CH-Tz (Figure S4). As shown in Figure 1d, the frontier orbital energy levels of the LUMO/HOMO were −3.58/−5.50 eV, −3.53/−5.61 eV, and −3.85/−5.77 eV for PM6, D18-Cl, and CH-Tz, respectively. Compared with PM6, D18-Cl possessed a deeper HOMO, which was beneficial for the device to obtain a higher V_{oc}. The energy offset between polymer donors and CH-Tz should be able to afford sufficient driving force for exciton dissociation—a key factor for obtaining a high J_{sc} [34].

Owing to the effective absorption properties and suitable energy levels of CH-Tz, we investigated its photovoltaic potentials as an electron acceptor. Thus, a series of OSCs was fabricated by adopting a conventional structure of indium tin oxides (ITO)/poly(3,4-ethyl-enedioxythiophene):poly(styrenesulfonate) (PEODT:PSS)/polymer donor:CH-Tz/poly[(9,9-bis(3′-(*N*,*N*-dimethylamino)propyl)-2,7-fluorene)-alt-5,5′-bis(2,2′-thiophene)-2,6-naphthalene-1,4,5,8-tetracaboxylic-*N*,*N*′-di(2-ethylhexyl)imide] (PNDIT-F3N)/Ag. The current density-voltage (*J*-*V*) curves of the CH-Tz-based devices were measured under AM 1.5G (100 mW cm^{-2}), and Table 1 lists the corresponding photovoltaic data. As shown in Figure 2a and Table 1, PM6- and D18-Cl-based devices achieved satisfactory PCEs exceeding 18% with an excellent J_{sc} above 27 mA cm^{-2}. Compared with D18-Cl-based devices, PM6-based devices exhibited a higher J_{sc} of 27.54 mA cm^{-2} and an improved FF above 80%, contributing to its slightly enhanced PCE of 18.54%. The V_{oc} of the

Table 1 Summary of photovoltaic parameters of OSCs. The average parameters in parentheses were calculated from 15 independent devices

Active layer	V_{oc} (V)	J_{sc} (mA cm^{-2})	J_{sc}^{EQE} (mA cm^{-2})	FF (%)	PCE (%)
PM6:CH-Tz	0.840 (0.839 ± 0.002)	27.54 (27.25 ± 0.22)	26.80	80.12 (79.78 ± 0.44)	18.54 (18.23 ± 0.18)
D18-Cl:CH-Tz	0.869 (0.867 ± 0.002)	27.11 (26.87 ± 0.28)	26.19	77.34 (77.30 ± 0.28)	18.23 (18.00 ± 0.14)
PM6:D18-Cl:CH-Tz	0.842 (0.844 ± 0.002)	28.15 (27.78 ± 0.24)	26.93	79.45 (79.61 ± 0.28)	18.85 (18.67 ± 0.10)
PM6:D18-Cl:CH-Tz:L8-BO	0.859 (0.859 ± 0.002)	27.72 (27.60 ± 0.14)	26.55	80.12 (79.91 ± 0.37)	19.09 (18.94 ± 0.06)

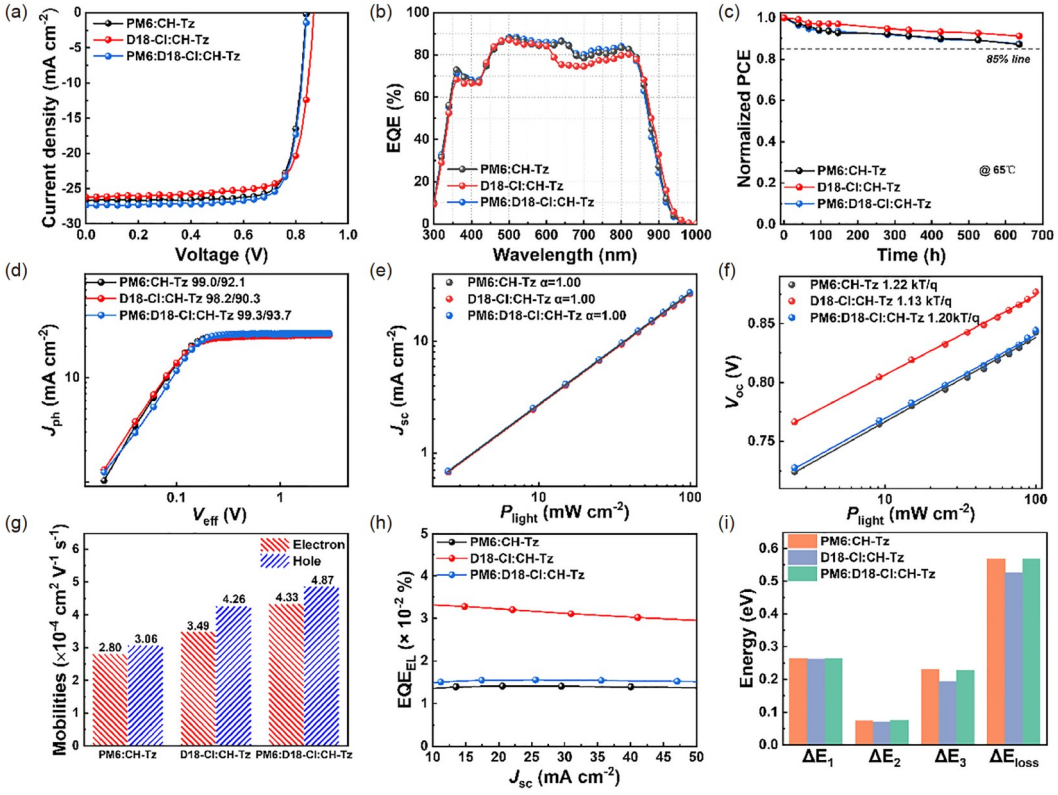

Figure 2 (a) *J-V* curves of CH-Tz-based OSCs. (b) EQE spectra of CH-Tz-based OSCs. (c) Thermal stability of CH-Tz-based OSCs without encapsulation in the nitrogen-filled glove box at 65 °C. (d) J_{ph}-V_{eff} curves of OSCs. (e) J_{sc} *vs.* light intensity of OSCs. (f) V_{oc} *vs.* light intensity of the OSCs. (g) Hole and electron mobilities of the OSCs. (h) EL quantum efficiencies of OSCs under different injected current densities. (i) E_{loss} and detailed three parts of ΔE_1, ΔE_2 and ΔE_3 values of OSCs (color online).

D18-Cl-based devices was ~0.03 V higher than that of the PM6-based devices, ascribable to its deeper HOMO energy level and reduced energy loss. Thus, D18-Cl was adopted as the third component in the host PM6:CH-Tz binary blend to further improve the device performance. Consequently, after optimizing the ratio of PM6 to that of D18-Cl, the PCE of the optimal ternary device using the PM6:D18-Cl:CH-Tz blend improved to 18.85% with a slightly higher V_{oc} of 0.842 V and an enhanced J_{sc} of 28.15 mA cm^{-2}. Compared with PM6:CH-Tz binary devices, the improved V_{oc} and J_{sc} of the ternary device were caused by the improved morphology of the active layer, as discussed below. The detailed optimal device parameters, including the device conformation, are summarized in Tables S1–S5 (Supporting Information online).

To verify the reliability of the J_{sc} values of the OSC devices, the external quantum efficiency (EQE) of the CH-Tz-based devices was measured, and Figure 2b shows the corresponding EQE curves. All the devices exhibited a broad photo-response from 300 to ~950 nm. The EQE response of the PM6:CH-Tz- and PM6:D18-Cl:CH-Tz-based devices exceeded 80% within the wavelength range of 450–800 nm, indicating a rather efficient photon-to-electron conversion in the corresponding devices. In addition, the ternary device exhibited a slightly higher EQE response practically across the entire photoresponse range, which explained its highest J_{sc}. The integrated J_{sc} values calculated from the EQE spectra were 26.80, 26.19, and 26.93 mA cm^{-2} for the PM6:CH-Tz-, D18-Cl:CH-Tz-, and PM6:D18-Cl:CH-Tz-based devices, respectively, following the same trend of the J_{sc} values ob-

tained from the *J*-*V* curves.

For high-performance OSCs, the evaluation of thermal stability is a critical factor in advancing the development of OSCs. Thus, the thermal stability of the CH-Tz-based devices was tested under continuous heating at 65 °C without encapsulation in a nitrogen-filled glove box. Figure 2c shows that all the CH-Tz-based devices demonstrated superior thermal stability, retaining ~85% of their initial PCE after thermal aging for 630 h. The good thermal stability may have been due to the effective and compact 3D molecular packing and the strong intermolecular potential of CH-Tz, as evidenced by single crystal XRD results [26,35,36].

To understand the exciton dynamics in CH-Tz-based blend films, steady-state photoluminescence (PL) measurement was conducted. As illustrated in Figure S5, all blend films exhibited much higher PL quenching efficiency, suggesting the efficient exciton dissociation process in OSCs devices. The outstanding J_{sc} values of the CH-Tz-based devices were associated with their charge dynamic properties, which can be investigated by measuring the dependence of the photocurrent density (J_{ph}) on the effective voltage (V_{eff}) (Figure 2d) [37]. Following the reported methods, the exciton dissociation efficiency (η_{diss}) was determined by $\eta_{diss} = J_{sc}/J_{sat}$, where J_{sat} is the saturated photocurrent density. The charge collection efficiency (η_{coll}) can be assessed from the ratio of $\eta_{coll} = J_{ph}/J_{sat}$, where J_{ph} is the photocurrent density at the maximum power output point. Thus, the PM6:CH-Tz-, D18-Cl:CH-Tz-, and PM6:D18-Cl:CH-Tz-based OSC devices afforded η_{diss}/η_{coll} values of 99.0%/92.1%, 98.2%/90.3%, and 99.3%/93.7%, respectively. The highest η_{diss}/η_{coll} of the PM6:D18-Cl:CH-Tz-based devices partly accounted for its J_{sc} exceeding 28 mA cm^{-2}. The dependence of the J_{sc} and V_{oc} on the light intensity (P_{light}) of the CH-Tz-based devices was measured to investigate the charge recombination. After fitting the J_{sc} and P_{light} data, all the devices were observed to exhibit the same α value of the unit (Figure 2e) [38], indicating the negligible bimolecular recombination of the CH-Tz-based devices. Figure 2f shows the relationship between the V_{oc} and P_{light}, where the slope values (n) of PM6:CH-Tz, D18-Cl:CH-Tz, and PM6:D18-Cl:CH-Tz was estimated at 1.22, 1.13, and 1.20, respectively. This suggested that the incorporation of D18-Cl in the PM6:CH-Tz-based binary device alleviated trap-assisted charge recombination.

The carrier transport properties of the CH-Tz-based OSC devices were measured through the space-charge-limited-current method (Figure S6), and Figure 2g shows the corresponding carrier mobilities of the devices. The electron mobility (μ_e) of CH-Tz was also measured to be 3.49×10^{-4} cm^2 V^{-1} s^{-1}, which could be attributed to its effective and compact 3D molecular packing and strong intermolecular potential as revealed by single crystal result. The electron mobility (μ_e) and hole mobility (μ_h) of the PM6:CH-Tz blend film were estimated at 2.80×10^{-4} and 3.06×10^{-4} cm^2 V^{-1} s^{-1}, respectively. This balance charge transport behavior was beneficial for realizing a high FF above 80% for the PM6:CH-Tz-based devices. After replacing PM6 with D18-Cl, the hole mobility improved to 4.26×10^{-4} cm^2 V^{-1} s^{-1}, which may have been related to the high crystallinity of D18-Cl. The addition of D18-Cl to the host PM6:CH-Tz blend promoted the μ_e and μ_h to 4.33×10^{-4} and 4.87×10^{-4} cm^2 V^{-1} s^{-1}, respectively. The best charge transport properties of the PM6:D18-Cl:CH-Tz ternary blend are considered the reason for its photovoltaic performance [39].

As previously mentioned, the D18-Cl-based device achieved a higher V_{oc} than the PM6-based device. Thus, a detailed energy loss analysis was conducted according to the reported balance theory [40]. First, their EQE values of electroluminescence (EQE_{EL}) were measured to evaluate the nonradiative energy loss (ΔE_3). As shown in Figure 2h, the D18-Cl:CH-Tz-based device exhibited an EQE_{EL} of 3.2×10^{-4}, which was higher than the PM6:CH-Tz-based device (1.4×10^{-4}). Thus, a smaller ΔE_3 of 0.193 eV was obtained for the D18-Cl-based device compared with that of the PM6-based device (0.230 eV). This played a vital role in their total energy losses and, in turn, V_{oc} values. Table S6 and Figure 2i summarize the detailed energy losses. The bandgaps (E_g) of the blend films were determined from Fourier-transform photocurrent spectroscopy (FTPS)-EQE spectra (Figure S7) [40,41]. The total energy losses for PM6-, D18-Cl-, and PM6:D18-Cl-based devices were 0.568, 0.527, and 0.567 eV, respectively. The PM6:CH-Tz- and PM6:D18-Cl:D18-Cl-based devices exhibited similar energy losses, whereas the D18-Cl-based devices exhibited the lowest energy losses.

Film morphology is another important factor that affects the PCE of OSC devices. To probe molecular packing behaviors in neat and blend films, grazing-incidence wide-angle X-ray scattering (GIWAXS) analysis was conducted [42]. Figures S8 and S9 show the 2D pattern of the films and the corresponding 1D line-cut profiles of the neat films, respectively. All the neat films exhibited a pronounced (010) diffraction peak in the out-of-plane (OOP) direction and sharp (100) diffraction peaks in the in-plane (IP) direction, suggesting their preferred face-on molecular orientations. All the neat films had similar coherence lengths (CLs) of (010) orientation of approximately 20 Å (Table S7). The GIWAXS patterns of the blend films (Figure 3a–c) showed that the films maintained a clear face-on orientation. This was evidenced by the (010) diffraction peak in the OOP direction and the (100) diffraction peak in the IP direction. The *d*-spacings and CLs of the (010) peaks in the OOP direction were 3.70 and 18.08 Å, 3.76 and 18.66 Å, and 3.75 and 18.47 Å for PM6:CH-Tz, D18-Cl:CH-Tz, and PM6:D18-Cl:CH-Tz, respectively (Figure 3d–f and Table S8). Owing to the addition of D18-Cl, the PM6:D18-Cl:CH-

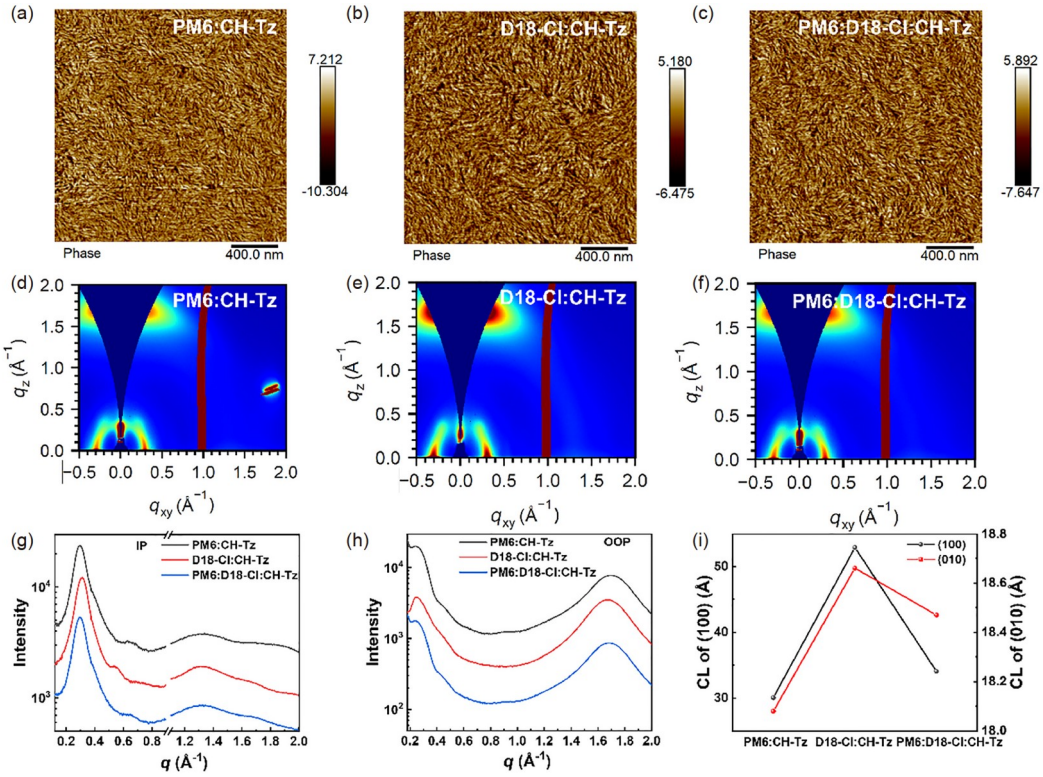

Figure 3 (a–c) AFM phase images of PM6:CH-Tz, D18-Cl:CH-Tz and PM6:D18-Cl:CH-Tz. (d–f) 2D GIWAXS patterns of the optimized blend films of PM6:CH-Tz, D18-Cl:CH-Tz and PM6:D18-Cl:CH-Tz. (g) Line cuts of GIWAXS images of the blend films in the in-plane (IP) direction. (f) Line cuts of GIWAXS images of the blend films in the out-of-plane (OOP) direction. (i) Coherence length of (100) and (010) in OOP direction for CH-Tz-based blend films (color online).

Tz blend films had larger CLs of (100) and (010) peaks than PM6:CH-Tz, which facilitated charge transport and reduced charge recombination.

Atomic force microscopy (AFM) was conducted to observe the phase separation of the blend films. The AFM phase images (Figure 3h–j) showed that the blend films exhibited distinct bi-continuous networks with bundle-like nanofibers, facilitating charge separation and transport. The appropriate phase separation size was conducive to exciton dissociation and charge transport, leading to better photovoltaic performance. Thus, a statistical size analysis of the nanofiber size was conducted. As shown in Figures S11 and S12, the diameter of the nanofibers was 23.7 ± 4.9 and 28.6 ± 7.7 nm for PM6:CH-Tz and D18-Cl:CH-Tz, respectively. The introduction of D18-Cl adjusted the phase separation size of PM6:CH-Tz such that PM6:D18-Cl:CH-Tz had a suitable phase separation size of 24.6 ± 5.2 nm, resulting in an improved photovoltaic parameter for OSCs. To account for the difference in the phase separation size of the active layer, the contact angle of the materials was measured to determine the surface tension (γ) and estimate the miscibility between polymer donors and CH-Tz (Figure S13). The Flory-Huggins interaction parameter, χ, is one of the parameters that assess the miscibility between the donor and acceptor [43]. A low χ implied better miscibility between the donor and acceptor, resulting in a small phase separation size. The χ values calculated by $\chi_{da} = K\left(\sqrt{\gamma_d} - \sqrt{\gamma_a}\right)^2$, where K is a proportionality constant, were 0.161, 0.251, and 0.179 K for the PM6:CH-Tz, D18-Cl:CH-Tz, and PM6:D18-Cl:CH-Tz blend films, respectively (Table S9). The medium miscibility for the PM6:D18-Cl:CH-Tz blend film may have accounted for the most suitable phase size separation.

Generally, OSCs with a good tolerance of active layer thickness are ideal for large-scale roll-to-roll printing [44,45]. Owing to the high crystallinity and mobility of CH-Tz [46], PM6:D18-Cl:CH-Tz-based OSC devices with different active layer thicknesses (~450 and ~560 nm) were fabricated. Figure 4a, b show their corresponding *J-V* curves and EQE profiles. As summarized in Table S10, when the thickness reached up to 560 nm, a decent PCE of 14.93% was still achieved for the CH-Tz-based OSC devices with a remarkable J_{sc} of 28.92 mA cm^{-2}. This was the highest J_{sc} for OSCs with a film thickness above 500 nm (Figure 4c and Table S11). Under this circumstance, the integrated J_{sc} of the CH-Tz-based thick film devices was 28.20 mA cm^{-2}, with a margin of less than 3%, supporting the aforementioned result. To further demonstrate the excellent photovoltaic performance of CH-Tz, a quaternary OSC device based on CH-Tz was prepared, and Figure S14 shows its optimal *J-V*

curve. The PM6:D18-Cl:CH-Tz:L8-BO quaternary device obtained a superior PCE of 19.09% with a V_{oc} of 0.859 V, high J_{sc} of 27.72 mA cm^{-2}, and FF of 80.12%. The integrated photocurrent values calculated from the EQE spectra were 26.55 mA cm^{-2} for the quaternary device, verifying the result obtained from *J-V* curve.

Finally, single crystal XRD was employed to reveal the molecular packing behaviors of CH-Tz. Table S12 lists the related structure parameters of the single crystal. All the alkyl chains were simplified to methyl groups for clear observation. The distance between the sulfur on the bridged thiophene and the nitrogen on the phenazine was approximately 3.2 Å (Figure S15). This was smaller than the sum van der Waals radii (~3.5 Å) of S and N [47], indicating an atypical non-covalent S···N secondary interaction. The distance of S···N was smaller than that of most NFAs, such as Y6 (~3.5 Å) [16], CH17 (~3.3 Å) [24], and CH22 (~3.4 Å) [35], implying that non-covalent S···N secondary interactions are the strongest in CH-Tz. This strong non-covalent secondary interaction can also guarantee planar and rigid conjugated backbones [26,48]. The overall view in Figure 5a shows that CH-Tz can establish a favorable 3D molecular packing network and possess rectangular voids of 30.74 Å × 30.48 Å. Subsequently, all the intermolecular packing modes with an intermolecular potential [49,50] above 100 kJ mol^{-1} were extracted from the single crystal of CH-Tz (Figure 5b). Figure S16 shows the corresponding intermolecular potential of all the intermolecular packing modes. Three major packing modes of CH-Tz are shown in Figure 5c and were similar to the packing modes of Y6. Mode 1 is the molecular packing mode that involves the "end group to end group" interaction. It is considered the E/E mode. Mode 2 is a dual packing mode between the end group and bridged thiophene, also called the "dual E/b mode". Mode 3, comprising both an end/end group and central/central unit ("E/E + C/C" mode), played an important role in forming the 3D packing network. Mode 3 of CH-Tz exhibited the largest intermolecular potential of approximately −263.5 kJ mol^{-1} compared with other packing modes. Importantly, CH-Tz exhibited a large total packing energy of

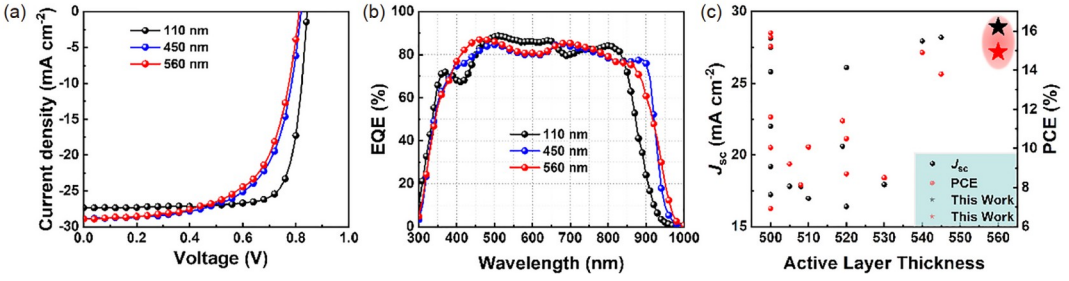

Figure 4 (a) *J-V* curves of PM6:D18-Cl:CH-Tz devices with different photoactive layer thickness. (b) EQE spectra of PM6:D18-Cl:CH-Tz devices with different photoactive layer thickness. (c) A summary of the PCE for thick-film OSCs with over 500 nm (color online).

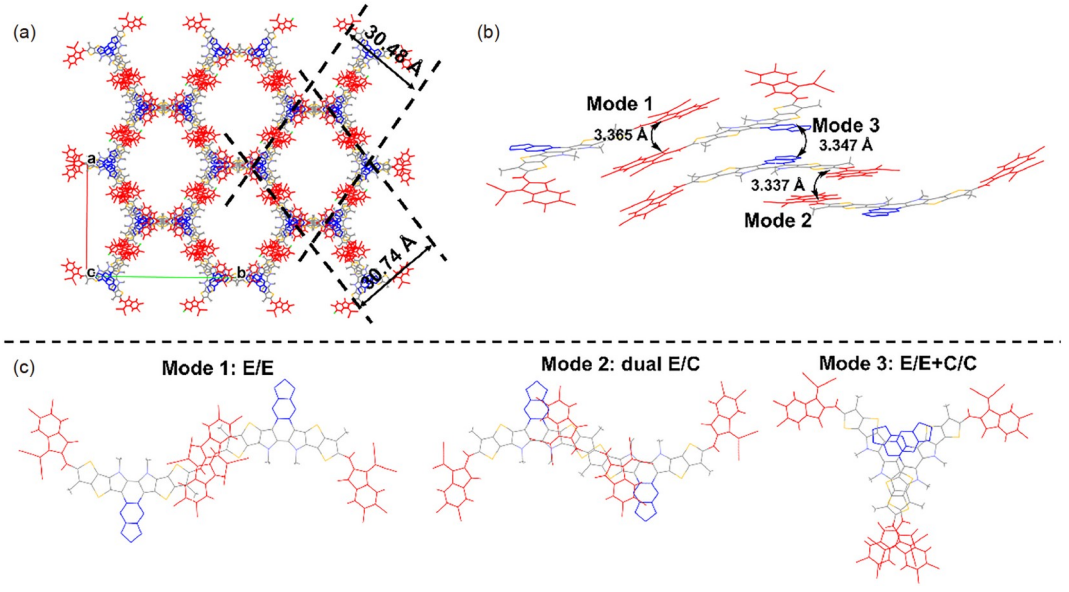

Figure 5 (a) Single-crystal packing images on the top view of CH-Tz. (b) The π-π interlayer distances between acceptor molecular layers include three types of intermolecular packing modes. (c) The three types of intermolecular packing modes of CH-Tz (color online).

−325.6 kJ mol^{-1}, which could facilitate the formation of more efficient molecular packing, resulting in a potentially superior OSC performance [24,35]. Effective 3D molecular packing and strong intermolecular potential were observed in CH-Tz with a 2D conjugation extended electron-deficient central unit. This led to more efficient 3D charge transport channels, high carrier mobility, reduced charge recombination and energy disorder, and, ultimately, a high PCE [16,26,35].

3 Conclusions

This study designed and constructed a new NFA of CH-Tz featuring a conjugation extended electron-deficient unit of [1,2,5]thiadiazolo[3,4-b]quinoxaline. CH-Tz exhibited near-infrared absorption, strong intermolecular interaction, and an effective 3D molecular packing network in its single crystal. After blending with PM6, the PM6:CH-Tz-based binary device achieved a high PCE of 18.54%, a J_{sc} of 27.54 mA cm^{-2}, and an excellent FF of 80.12%. Morphological analysis revealed a uniform phase separation morphology with a distinct bi-continuous network in the blend film. The addition of D18-Cl further optimized the molecular packing and crystallinity, leading to higher charge transport mobilities and, thus, better device performance. Ternary devices with D18-Cl as the third component and quaternary devices with L8-BO as the fourth component achieved enhanced PCEs of 18.85% and 19.09%, respectively. Importantly, a remarkable PCE of 14.93% was achieved for the CH-Tz-based OSC devices and an unparalleled J_{sc} of 28.92 mA cm^{-2} was obtained when the thickness of the active layers was 560 nm. With its excellent thermal stability, CH-Tz-based devices exhibited significant potential toward efficient and stable OSCs. This study advances the strong influence of central units on molecular photovoltaic properties and guides the design of acceptors for stable and large-thickness OSCs.

Acknowledgements This work was supported by the Ministry of Science and Technology of China (2022YFB4200400, 2019YFA0705900, 2023YFE0210400), the National Natural Science Foundation of China (21935007, 52025033, 52303237, 22361132530). The authors thank Yu Chen at the Beijing Synchrotron Radiation Facility, Institute of High Energy Physics for performing GIWAXS measurements.

Conflict of interest The authors declare no conflict of interest.

Supporting information The supporting information is available online at chem.scichina.com and link.springer.com/journal/11426. The supporting materials are published as submitted, without typesetting or editing. The responsibility for scientific accuracy and content remains entirely with the authors.

1 Zhang G, Lin FR, Qi F, Heumüller T, Distler A, Egelhaaf HJ, Li N, Chow PCY, Brabec CJ, Jen AKY, Yip HL. *Chem Rev*, 2022, 122: 14180–14274
2 Zhang G, Zhao J, Chow PCY, Jiang K, Zhang J, Zhu Z, Zhang J, Huang F, Yan H. *Chem Rev*, 2018, 118: 3447–3507
3 Dou L, Liu Y, Hong Z, Li G, Yang Y. *Chem Rev*, 2015, 115: 12633–12665
4 Nielsen CB, Holliday S, Chen HY, Cryer SJ, McCulloch I. *Acc Chem Res*, 2015, 48: 2803–2812
5 Duan T, Chen Q, Hu D, Lv J, Yu D, Li G, Lu S. *Trends Chem*, 2022, 4: 773–791
6 Chen T, Li S, Li Y, Chen Z, Wu H, Lin Y, Gao Y, Wang M, Ding G, Min J, Ma Z, Zhu H, Zuo L, Chen H. *Adv Mater*, 2023, 35: 2300400
7 Zhu L, Zhang M, Xu J, Li C, Yan J, Zhou G, Zhong W, Hao T, Song J, Xue X, Zhou Z, Zeng R, Zhu H, Chen CC, MacKenzie RCI, Zou Y, Nelson J, Zhang Y, Sun Y, Liu F. *Nat Mater*, 2022, 21: 656–663
8 Jiang K, Zhang J, Zhong C, Lin FR, Qi F, Li Q, Peng Z, Kaminsky W, Jang SH, Yu J, Deng X, Hu H, Shen D, Gao F, Ade H, Xiao M, Zhang C, Jen AKY. *Nat Energy*, 2022, 7: 1076–1086
9 Zheng Z, Wang J, Bi P, Ren J, Wang Y, Yang Y, Liu X, Zhang S, Hou J. *Joule*, 2022, 6: 171–184
10 Wang J, Zheng Z, Bi P, Chen Z, Wang Y, Liu X, Zhang S, Hao X, Zhang M, Li Y, Hou J. *Natl Sci Rev*, 2023, 10: nwad085
11 Wang L, Chen C, Fu Y, Guo C, Li D, Cheng J, Sun W, Gan Z, Sun Y, Zhou B, Liu C, Liu D, Li W, Wang T. *Nat Energy*, 2024, doi: 10.1038/s41560-023-01436-z
12 Gan Z, Wang L, Cai J, Guo C, Chen C, Li D, Fu Y, Zhou B, Sun Y, Liu C, Zhou J, Liu D, Li W, Wang T. *Nat Commun*, 2023, 14: 6297
13 Liu C, Fu Y, Zhou J, Wang L, Guo C, Cheng J, Sun W, Chen C, Zhou J, Liu D, Li W, Wang T. *Adv Mater*, 2024, 36: 2308608
14 Zhou J, Li D, Wang L, Zhang X, Deng N, Guo C, Chen C, Gan Z, Liu C, Sun W, Liu D, Li W, Li Z, Wang K, Wang T. *Interdisc Mater*, 2023, 2: 866–875
15 Zhu L, Tu Z, Yi Y, Wei Z. *J Phys Chem Lett*, 2019, 10: 4888–4894
16 Zhu W, Spencer AP, Mukherjee S, Alzola JM, Sangwan VK, Amsterdam SH, Swick SM, Jones LO, Heiber MC, Herzing AA, Li G, Stern CL, DeLongchamp DM, Kohlstedt KL, Hersam MC, Schatz GC, Wasielewski MR, Chen LX, Facchetti A, Marks TJ. *J Am Chem Soc*, 2020, 142: 14532–14547
17 Aldrich TJ, Matta M, Zhu W, Swick SM, Stern CL, Schatz GC, Facchetti A, Melkonyan FS, Marks TJ. *J Am Chem Soc*, 2019, 141: 3274–3287
18 Zhu L, Zhang M, Zhou G, Hao T, Xu J, Wang J, Qiu C, Prine N, Ali J, Feng W, Gu X, Ma Z, Tang Z, Zhu H, Ying L, Zhang Y, Liu F. *Adv Energy Mater*, 2020, 10: 1904234
19 Li C, Zhou J, Song J, Xu J, Zhang H, Zhang X, Guo J, Zhu L, Wei D, Han G, Min J, Zhang Y, Xie Z, Yi Y, Yan H, Gao F, Liu F, Sun Y. *Nat Energy*, 2021, 6: 605–613
20 Zhu L, Zhang J, Guo Y, Yang C, Yi Y, Wei Z. *Angew Chem Int Ed*, 2021, 60: 15348–15353
21 Yuan J, Zhang H, Zhang R, Wang Y, Hou J, Leclerc M, Zhan X, Huang F, Gao F, Zou Y, Li Y. *Chem*, 2020, 6: 2147–2161
22 Han G, Yi Y. *Acc Chem Res*, 2022, 55: 869–877
23 Shoaee S, Luong HM, Song J, Zou Y, Nguyen T, Neher D. *Adv Mater*, 2023, 2302005
24 Chen H, Zou Y, Liang H, He T, Xu X, Zhang Y, Ma Z, Wang J, Zhang M, Li Q, Li C, Long G, Wan X, Yao Z, Chen Y. *Sci China Chem*, 2022, 65: 1362–1373
25 Chen H, Liang H, Guo Z, Zhu Y, Zhang Z, Li Z, Cao X, Wang H, Feng W, Zou Y, Meng L, Xu X, Kan B, Li C, Yao Z, Wan X, Ma Z, Chen Y. *Angew Chem Int Ed*, 2022, 61: e202209580
26 Lv X, Liu Z, Yang C, Ji Y, Zheng G. *Acc Mater Res*, 2023, 4: 264–274
27 Zou Y, Chen H, Bi X, Xu X, Wang H, Lin M, Ma Z, Zhang M, Li C, Wan X, Long G, Zhaoyang Y, Chen Y. *Energy Environ Sci*, 2022, 15: 3519–3533
28 Yao Z, Cao X, Bi X, He T, Li Y, Jia X, Liang H, Guo Y, Long G, Kan B, Li C, Wan X, Chen Y. *Angew Chem Int Ed*, 2023, 62: e202312630
29 Duan T, Feng W, Li Y, Li Z, Zhang Z, Liang H, Chen H, Zhong C,

Jeong S, Yang C, Chen S, Lu S, Rakitin OA, Li C, Wan X, Kan B, Chen Y. *Angew Chem Int Ed*, 2023, 62: e202308832
30 Wen T, Liu Z, Chen Z, Zhou J, Shen Z, Xiao Y, Lu X, Xie Z, Zhu H, Li C, Chen H. *Angew Chem Int Ed*, 2021, 60: 12964–12970
31 Spano FC. *Acc Chem Res*, 2009, 43: 429–439
32 Más-Montoya M, Janssen RAJ. *Adv Funct Mater*, 2017, 27: 1605779
33 Cao X, Guo J, Li Z, Bi X, Liang H, Xiao Z, Guo Y, Jia X, Xu Z, Ma K, Yao Z, Kan B, Wan X, Li C, Chen Y. *ACS Energy Lett*, 2023, 8: 3494–3503
34 Clarke TM, Durrant JR. *Chem Rev*, 2010, 110: 6736–6767
35 Liang H, Bi X, Chen H, He T, Lin Y, Zhang Y, Ma K, Feng W, Ma Z, Long G, Li C, Kan B, Zhang H, Rakitin OA, Wan X, Yao Z, Chen Y. *Nat Commun*, 2023, 14: 4707
36 Wu M, Ma B, Li S, Han J, Zhao W. *Adv Funct Mater*, 2023, 33: 2305445
37 Zhang K, Liu Z, Wang N. *J Power Sources*, 2019, 413: 391–398
38 Cowan SR, Roy A, Heeger AJ. *Phys Rev B*, 2010, 82: 245207
39 Proctor CM, Love JA, Nguyen TQ. *Adv Mater*, 2014, 26: 5957–5961
40 Rau U, Blank B, Müller TCM, Kirchartz T. *Phys Rev Appl*, 2017, 7: 044016
41 Wang Y, Qian D, Cui Y, Zhang H, Hou J, Vandewal K, Kirchartz T, Gao F. *Adv Energy Mater*, 2018, 8: 1801352
42 Xiao Y, Lu X. *Mater Today Nano*, 2019, 5: 100030
43 Kouijzer S, Michels JJ, van den Berg M, Gevaerts VS, Turbiez M, Wienk MM, Janssen RAJ. *J Am Chem Soc*, 2013, 135: 12057–12067
44 Li X, Pan F, Sun C, Zhang M, Wang Z, Du J, Wang J, Xiao M, Xue L, Zhang ZG, Zhang C, Liu F, Li Y. *Nat Commun*, 2019, 10: 519
45 Zhang J, Tan CH, Zhang K, Jia T, Cui Y, Deng W, Liao X, Wu H, Xu Q, Huang F, Cao Y. *Adv Energy Mater*, 2021, 11: 2102559
46 Zhang Y, Feng H, Meng L, Wang Y, Chang M, Li S, Guo Z, Li C, Zheng N, Xie Z, Wan X, Chen Y. *Adv Energy Mater*, 2019, 9: 1902688
47 De P, Roy K. *Struct Chem*, 2021, 32: 631–642
48 Wang L, An Q, Yan L, Bai HR, Jiang M, Mahmood A, Yang C, Zhi H, Wang JL. *Energy Environ Sci*, 2022, 15: 320–333
49 Gavezzotti A, Filippini G. *J Phys Chem*, 1994, 98: 4831–4837
50 Gavezzotti A. *Acc Chem Res*, 1994, 27: 309–314